Commun. Comput. Phys.
doi: 10.4208/cicp.2014.m391

Vol. **17**, No. 5, pp. 1127-1150
May 2015

Unified Gas Kinetic Scheme and Direct Simulation Monte Carlo Computations of High-Speed Lid-Driven Microcavity Flows

Vishnu Venugopal and Sharath S. Girimaji*

Department of Aerospace Engineering, Texas A&M University, College Station, TX-77843, United States of America.

Received 5 December 2013; Accepted (in revised version) 11 April 2014

Abstract. Accurate simulations of high-speed rarefied flows present many physical and computational challenges. Toward this end, the present work extends the Unified Gas Kinetic Scheme (UGKS) to a wider range of Mach and Knudsen numbers by implementing WENO (Weighted Essentially Non-Oscillatory) interpolation. Then the UGKS is employed to simulate the canonical problem of lid-driven cavity flow at high speeds. Direct Simulation Monte Carlo (DSMC) computations are also performed when appropriate for comparison. The effect of aspect ratio, Knudsen number and Mach number on cavity flow physics is examined leading to important insight.

AMS subject classifications: 82C40, 76P04, 65C05

Key words: UGKS, DSMC, lid driven cavity, kinetic theory, Knudsen number.

1 Introduction

High-speed rarefied microcavity flows are of importance in the study of hypersonic flight and atmospheric re-entry flows. Scratches, impact damage or manufacturing defects in the thermal protection system of the flight vehicles can be conveniently modeled as microcavities. The presence of a microcavity on the thermal protection system surface may potentially be hazardous. According to Bertin and Cummings [1], one of the main contributing factors to the Columbia space shuttle accident was hot gas breaching through a cavity in the thermal protection system of the vehicle during its re-entry, causing catastrophic damage. Many of these flows of interest exhibit a wide range a Knudsen numbers within the flow domain of interest. For example, in high-altitude hypersonic and re-entry

*Corresponding author. *Email addresses:* vishnuv@tamu.edu (V. Venugopal), girimaji@tamu.edu (S. S. Girimaji)

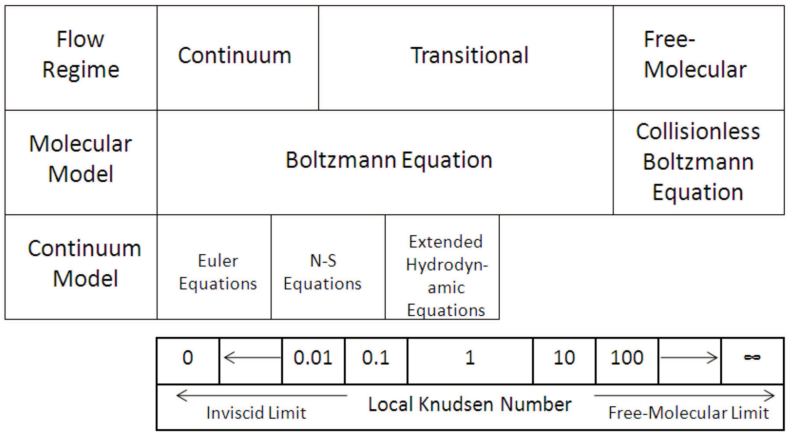

Figure 1: Knudsen number limits on the mathematical models.

flows, the freestream may be rarefied but the flow in the cavity could be close to continuum due to the entrapment of many molecules. It is important to characterize mixing and heat exchange efficiency of a cavity of given shape and size as functions of Reynolds, Mach and Knudsen numbers. Therefore, it is critical that the simulation tool be capable of capturing a range of Mach number and Knudsen number physics within a single flow domain.

Different Knudsen number regimes and corresponding physical features and governing equations are shown in Fig. 1. Efforts have been made in literature to couple continuum and discrete solvers to derive a hybrid scheme or even to extend the Boltzmann equation based solvers to continuum regime. However, the restrictions on time-step (of the order of mean collision time) and grid size (of the order of mean-free path) cannot be avoided because of the operator-splitting methods used for separating the collision and transport phenomena. The UGKS of Xu [2], is potentially efficient in both rarefied and continuum regimes due to the novel approach of coupling between particle transport and collision. The finite-volume UGKS evaluates the flux across each numerical cell according to the BGK-Shakhov [3,4] model with a discretized velocity space [5]. The advantage of UGKS is due to the fact that the time-step and the cell size are restricted by the Courant-Friedrichs-Lewy (CFL) condition rather than the corresponding mean collision time or mean-free path.

The main objectives of the paper are to: (i) extend the applicability of UGKS by implementing, testing and verifying a WENO (weighted essentially non-oscillatory) interpolation scheme; and (ii) examine the effect of Mach number, Knudsen number and aspect ratio on the flow characteristics in a lid-driven microcavity flow. In the first part, various WENO [6, 7] variants are compared against the original Van Leer [8] scheme to establish the applicability of the different interpolation schemes. Then the UGKS is compared against the well-established DSMC solver OpenFOAM (dsmcFOAM) at high Knudsen numbers. Once the verification is complete, the UGKS solver is used to investi-

gate the flow features within a microcavity at different conditions. This work addresses mostly two-dimensional flows for ease of numerical scheme development and verification/validation. Clearly further three-dimensional studies are needed for compete investigation of flow physics.

In Section 2, the basic features of DSMC and UGKS are discussed. Then the implementation of WENO for performing the interpolation required in UGKS reconstruction is presented. The cavity flow configuration and simulation parameters are described in Section 3. The results are presented in Section 4. The first set of results pertains to assessing the different WENO schemes and verification against DSMC. Then the flow physics in the cavity is examined as a function of relevant parameters. The paper concludes in Section 5 with a brief discussion.

2 DSMC and UGKS approaches

The physical underpinnings of DSMC and UGKS are briefly reviewed in this section. A detailed algorithm can be found in [9] and [2] for DSMC and UGKS schemes respectively. The implementation of WENO schemes into UGKS is discussed.

2.1 DSMC

The DSMC method represents real gas flow using a large number of simulated particles. This method is one way to realize physical processes modeled by the Boltzmann equation. The DSMC method, similar to other Monte Carlo schemes, is a statistical approach whose solutions are shown to converge towards the analytical solutions of Boltzmann equation with sufficiently large number of samples. The number of simulated molecules is much smaller than the number of real molecules present in the flow. Appropriate choice of collision partners and effecting sufficient number of collisions during one time step in a cell guarantees a reasonable facsimile of the real flow. The intermolecular collisions are treated on a probabilistic rather than a deterministic basis and are subject to the 'molecular chaos' ansatz. The essential DSMC approximation is the uncoupling, over a small time interval or step, of molecular streaming and intermolecular collisions. The position coordinates, velocity components and internal state of each molecule evolve in time subject to representative collisions within the domain and due to boundary interactions.

A typical DSMC implementation can be briefly described as follows. A physical flow domain with appropriate boundaries is described. The computational domain is divided into cells used for selecting collision partners and over which the particle properties are averaged to obtain macroscopic properties. The physical domain is initialized by specifying the number of simulated particles and assigning initial position and velocity values according to an equilibrium probability density function calculated from the given flow conditions. The simulation then proceeds, stepping through time as follows:

1. The particles are advected according to the velocity and time step size.
2. Boundary conditions, such as collisions with walls, inflow and outflow, are applied.
3. Particle collisions (elastic and inelastic) are computed based on collision probabilities and molecular models.
4. Macroscopic flow field variables are evaluated by averaging over the properties of the individual particles.

This procedure implies certain assumptions and limitations. First, the time step must be small enough relative to the mean collision time such that the particle movements and the collision operations can be separated. This entails the time step to be approximately one-third of the mean collision time. Second, the collision partners are chosen among the particles in each cell. Consequently, each cell should be less than one mean-free path in size. Collision partners can then be randomly chosen from the particles in each cell while maintaining physical accuracy. Third, each cell should contain sufficient particles such that the macroscopic averages are statistically meaningful. Generally 20 to 25 particles per cell are required. Further, when the mean flow speed is much lesser than the corresponding molecular speed, the DSMC method is subject to significant statistical fluctuations. By its very nature, DSMC is well suited for high-speed rarefied flows. However, those very features render DSMC computationally expensive for continuum, near-continuum or low-speed flows. More details on DSMC can be found in [9].

2.2 UGKS

The Unified Gas Kinetic Scheme (UGKS) proposes an alternate approach to solving the Boltzmann equation. The UGKS is based on GKM (Gas Kinetic Method) which has been successfully used in the continuum regime [10–13]. UGKS is a finite volume approach wherein the fluxes through the control surfaces are derived from the BGK-Shakhov model [3, 4] with a discretized velocity space [5]. The BGK-Shakhov model equation for one dimensional case (for simplicity) can be written as:

$$\partial_t f + u\partial_x f = \frac{f^{+(0)} - f}{\tau}, \tag{2.1}$$

where f is the single particle velocity distribution function (vdf), u is the particle velocity, τ is the mean collision time and $f^{+(0)}$ is the modified (due to Prandtl number fix [3]) equilibrium velocity distribution function (vdf). The modified equilibrium distribution is expressed as:

$$f^{+(0)} = f^{(0)}\left[1+(1-Pr)\,\mathbf{c}.\mathbf{q}\left(\frac{c^2}{RT}-5\right)/\left(5pRT\right)\right], \tag{2.2}$$

where $f^{(0)}$ is the Maxwellian distribution, Pr is the Prandtl number, $\mathbf{c}$ is the random (or thermal or peculiar) velocity, $\mathbf{q}$ is the heat flux, R is the gas constant and T is the

temperature. The Maxwellian distribution for 1-D case is:

$$f^{(0)}=\rho\left(\frac{\lambda}{\pi}\right)^{\frac{K+1}{2}}e^{-\lambda\left((u-U)^2-\zeta^2\right)}, \tag{2.3}$$

where ρ is the density, $\lambda=m/(2k_BT)$, m is the molecular mass, k_B is the Boltzmann constant, U is the macroscopic velocity, K is the number of internal degrees of freedom and $\zeta^2=\sum_{i=1}^{K}\zeta_i^2$ is the energy associated with the internal degrees of freedom.

An integral solution of the BGK-Shakhov equation constructed via the method of characteristics [14] is:

$$f(x,t,u,\zeta)=\frac{1}{\tau}\int_{t^n}^{t^{n+1}}f^{(0)}\left(x-u\left(t-t^{'}\right),t^{'},u,\zeta\right)e^{\frac{t^{'}-t}{\tau}}dt^{'}+e^{\frac{t^n-t}{\tau}}f_0^n\left(x-u\left(t-t^n\right),t^n,u,\zeta\right), \tag{2.4}$$

where f_0^n is the initial distribution function at t^n.

The implementation of the finite volume method starts with the discretization of the physical, temporal and the particle velocity space which is collectively known as the phase space.

1. The physical space is divided into uniform structured cells where the i^{th} cell has its center at x_i and its left and right interfaces are denoted by $x_{i-1/2}$ and $x_{i+1/2}$ respectively. Hence the cell size $\Delta x_i=x_{i+1/2}-x_{i-1/2}$.

2. The discretized temporal space is represented by t^n for the n^{th} time-step.

3. The velocity space is divided into $2M+1$ cells with the cell size Δu. The center of k^{th} velocity interval is $u_k=k\Delta u_k$. Hence, the cell averaged particle velocity at the k^{th} cell
$$u_k\in\left[\left(k-\frac{1}{2}\right)\Delta u_k,\left(k+\frac{1}{2}\right)\Delta u_k\right];\quad k\in\mathbb{Z}[-M,M]. \tag{2.5}$$

Using finite volume discretization in phase space and invoking the trapezoidal rule to approximate the collision term, the BGK-Shakhov difference equation takes the form:

$$f_{i,k}^{n+1}=f_{i,k}^n+\frac{1}{\Delta x}\int_{t^n}^{t^{n+1}}\left(f_{i-1/2,k}u_k-f_{i+1/2,k}u_k\right)dt+\frac{\Delta t}{2}\left(\frac{f_{i,k}^{+(0)(n+1)}-f_{i,k}^{n+1}}{\tau^{n+1}}+\frac{f_{i,k}^{+(0)(n)}-f_{i,k}^n}{\tau^n}\right), \tag{2.6}$$

where $f_{i,k}^n$ and $f_{i,k}^{n+1}$ are the cell averaged distribution functions in the i^{th} cell and k^{th} discrete particle velocity (u_k), at t^n and t^{n+1} respectively. Here, Δx is the cell size and Δt is the time-step determined by CFL condition; $f_{i-1/2,k}$ and $f_{i+1/2,k}$ are the distribution functions across the cell interface which are computed using the integral solution of BGK-Shakhov equation (2.4). In the original UGKS, Van-Leer interpolation is used to determine the distribution (f_0^n in Eq. (2.4)) at a particular cell interface. The Maxwellian distribution ($f^{(0)}$ in Eq. (2.4)) across the cell interface is approximated by Taylor's expansion in space and

time. First order expansion of an equilibrium state is necessary to ensure the validity of UGKS over the entire Knudsen number regime. $f_{i,k}^{+(0)}$ and τ are modified equilibrium distributions and particle collision time respectively. Both quantities have a one-to-one correspondence with the instantaneous macroscopic properties. An evolution equation for the macroscopic properties can be obtained by taking the moments of the above BGK-Shakhov difference equation about the collision invariants ($\boldsymbol{\psi}$):

$$\boldsymbol{\psi}=\left(1,u,0.5\left(u^2+\zeta^2\right)\right)^T. \tag{2.7}$$

Note that the moments of collision terms about the collision invariants must vanish in order to satisfy conservation laws.

$$\mathbf{Q}_i^{n+1}=\mathbf{Q}_i^n+\frac{1}{\Delta x}\left(\mathbf{F}_{i-1/2}-\mathbf{F}_{i+1/2}\right), \tag{2.8}$$

where

$$\mathbf{F}=\int_{t^n}^{t^{n+1}}\int \boldsymbol{\psi} f u d\Xi dt, \quad \mathbf{Q}=\begin{pmatrix}\rho\\ \rho U\\ \rho E\end{pmatrix}, \quad d\Xi=du d\zeta_1 d\zeta_2\cdots d\zeta_k. \tag{2.9}$$

WENO Implementation

One of the crucial operations in the UGKS is the interpolation of the distribution function to the cell interface. In high Mach number flows, interpolation can be challenging due to the presence of steep shocks. It is shown that Van-Leer interpolation produces spurious oscillations in the computed results at high Knudsen number as well. In this work, we present the implementation of 5^{th} order WENO (Weighted Essentially Non-Oscillatory) schemes for interpolation [6, 7]. WENO uses a convex combination of all the candidate stencils neighbouring a cell, each being assigned a non-linear weight which depends on the local smoothness of the numerical solution based on the corresponding stencil. This ensures non-oscillatory behaviour near discontinuities without compromising the higher accuracy.

Fig. 2 shows a typical computational stencil used for each reconstruction scheme. A second order Van-Leer limiter uses the values stored at the immediate nodes neighbouring a cell interface to construct the value at the cell interface. For instance, the flux of the initial distribution function at k^{th} velocity space at the right interface of i^{th} cell is given by

$$q_{i+1/2,k}=q_{i,k}+(x_{i+1/2}-x_i)s_{i,k}, \tag{2.10}$$

where the slope $s_{i,k}$ is calculated from the Van-Leer scheme

$$s_{i,k}=(sign(s_1)+sign(s_2))\frac{|s_1||s_2|}{|s_1|+|s_2|}, \tag{2.11}$$

where

$$s_1=\frac{q_{i,k}-q_{i-1,k}}{x_i-x_{i-1}} \quad \text{and} \quad s_2=\frac{q_{i+1,k}-q_{i,k}}{x_{i+1}-x_i}. \tag{2.12}$$

Table 1: Variants of UGKS code.

Name	**Reconstruction scheme**
Van-Leer	2^{nd} order Van Leer limiter
WENO-S	5^{th} order WENO scheme of Shu [6]
WENO-C	5^{th} order WENO scheme of Carpenter [7]

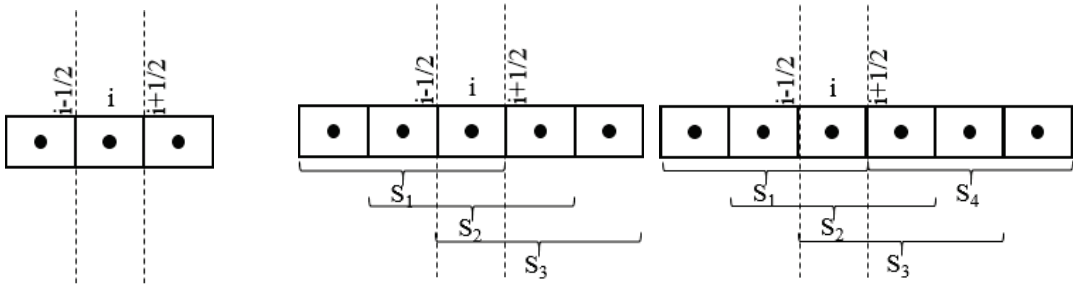

(a) Van-Leer (b) WENO-S (c) WENO-C

Figure 2: Computational stencils for different reconstruction schemes.

WENO-S scheme initially reconstructs the three values at the cell interface using the illustrated stencils S_1, S_2 and S_3. The final value at interface is then a convex combination of these values which are computed using weights that are specific for the scheme. WENO-C scheme is similar to WENO-S but avoids the bias of choosing three cells to the left of the interface and two from the right. Reconstruction based on this scheme can be computationally expensive as it involves calculations based on four stencils compared to that of WENO-S which uses only three stencils. However, WENO-C is known to lead to faster convergence [7].

WENO-S and WENO-C

The WENO-C scheme is presented first and WENO-S can be derived from WENO-C with minor simplifications. WENO-C calculates the numerical flux (flux of initial distribution function in our case) at the interface ($x_{i+\frac{1}{2}}$) as a convex combination of four third order fluxes that are calculated based on the following three point stencils: $S^{(1)}=\{x_{i-2},x_{i-1},x_i\}$, $S^{(2)}=\{x_{i-1},x_i,x_{i+1}\}$, $S^{(3)}=\{x_i,x_{i+1},x_{i+2}\}$ and $S^{(4)}=\{x_{i+1},x_{i+2},x_{i+3}\}$. Note that the collection of all four stencils is symmetric with respect to $x_{i+\frac{1}{2}}$. The WENO-C flux of any quantity q is then given by

$$q_{i+\frac{1}{2}}=w^{(1)}q^{(1)}_{i+\frac{1}{2}}+w^{(2)}q^{(2)}_{i+\frac{1}{2}}+w^{(3)}q^{(3)}_{i+\frac{1}{2}}+w^{(4)}q^{(4)}_{i+\frac{1}{2}}, \tag{2.13}$$

where $q^{(r)}_{i+\frac{1}{2}}$ is the 3^{rd} order flux defined by the stencil $S^{(r)}$ ($r=1,2,3,4$)

$$\begin{pmatrix} q^{(1)}_{i+\frac{1}{2}} \\ q^{(2)}_{i+\frac{1}{2}} \\ q^{(3)}_{i+\frac{1}{2}} \\ q^{(4)}_{i+\frac{1}{2}} \end{pmatrix} = \frac{1}{6} \begin{pmatrix} 2 & -7 & 11 & 0 & 0 & 0 \\ 0 & -1 & 5 & 2 & 0 & 0 \\ 0 & 0 & 2 & 5 & -1 & 0 \\ 0 & 0 & 0 & 11 & -7 & 2 \end{pmatrix} \begin{pmatrix} q_{i-2} \\ q_{i-1} \\ q_i \\ q_{i+1} \\ q_{i+2} \\ q_{i+3} \end{pmatrix} \tag{2.14}$$

and the weight function is given by

$$w^{(r)} = \frac{b^{(r)}}{\sum_{m=1}^{4} b^{(r)}}, \tag{2.15}$$

$$b^{(r)} = d^{(r)} \left(1 + \frac{p}{\epsilon + \beta^{(r)}} \right), \quad \epsilon = 10^{-6}, \tag{2.16}$$

$$d^{(1)} = \frac{1}{10} - \Delta, \quad d^{(2)} = \frac{6}{10} - 3\Delta, \quad d^{(3)} = \frac{3}{10} + 3\Delta, \quad d^{(4)} = \Delta. \tag{2.17}$$

The functions $\beta^{(r)}$ are the smoothness indicators and are given by

$$\beta^{(1)} = \frac{13}{12}(q_{i-2} - 2q_{i-1} + q_i)^2 \quad + \frac{1}{4}(q_{i-2} - 4q_{i-1} + 3q_i)^2, \tag{2.18a}$$

$$\beta^{(2)} = \frac{13}{12}(q_{i-1} - 2q_i + q_{i+1})^2 \quad + \frac{1}{4}(q_{i-1} - q_{i+1})^2, \tag{2.18b}$$

$$\beta^{(3)} = \frac{13}{12}(q_i - 2q_{i+1} + q_{i+2})^2 \quad + \frac{1}{4}(3q_i - 4q_{i+1} + 3q_{i+2})^2, \tag{2.18c}$$

$$\beta^{(4)} = \frac{13}{12}(q_{i+1} - 2q_{i+2} + q_{i+3})^2 + \frac{1}{4}(-5q_{i+1} + 8q_{i+2} - 3q_{i+3})^2. \tag{2.18d}$$

Simulations in 2-D physical space must be performed carefully. Apart from grid sensitivity studies, it is equally important to confirm that one is not missing to capture any three dimensional flow features. Possibility of 3-D effects are high in our case since we deal with highly non-equilibrium flows with multiple vortex structures. However, in the following part, it is seen that our flow structures are free from any 3-D effects ensuring accurate results with corresponding 2-D simulations. The expression for p is given by

$$p = \begin{cases} (-q_{i-2} + 5q_{i-1} - 10q_i + 10q_{i+1} - 5q_{i+2} + q_{i+3})^2, & \text{for } \Delta \neq 0, \\ (q_{i-2} - 4q_{i-1} + 6q_i - 4q_{i+1} + q_{i+2})^2, & \text{for } \Delta = 0. \end{cases} \tag{2.19}$$

The value of Δ affects the convergence rate and for the specific value of $\Delta_c = \frac{1}{20}$, the convergence rate is 6 [7]. All our WENO-C simulations are with $\Delta = \frac{1}{20}$. It can be proved that the classical fifth-order upwind-biased WENO-S scheme of Shu [6] is obtained by

setting $\Delta = 0$. It should be noted that the WENO reconstruction to the left interface to obtain $q_{i-\frac{1}{2}}$ is mirror symmetric with respect to x_i of the above procedure [6].

The flux of the initial distribution function at the cell interface at $x_{i+1/2}$ is selected based on the direction of the mean particle velocity in the corresponding velocity space u_k:

$$q_{i+1/2,k} = \begin{cases} q^{(left)}_{i+1/2,k}, & \text{if } u_k \geq 0, \\ q^{(right)}_{i+1/2,k}, & \text{if } u_k < 0. \end{cases} \tag{2.20}$$

3 Cavity flow simulation

We simulate the flow of Argon gas within a cavity driven by a lid moving at a constant velocity of U_{lid}. The degree of rarefaction is set using the global (freestream) Knudsen number, which is the ratio between the mean-free path of the molecules in the freestream (λ_∞) to the global length scale (L).

$$Kn_{global} = \frac{\lambda_\infty}{L}. \tag{3.1}$$

Global length scale for this problem is defined as the characteristic width of the cavity, which is of the order of one micron. Hence, a 2D square cavity, would have the dimensions of $10^{-6}m \times 10^{-6}m$ (Fig. 3). All cavity walls including the lid are set to be isothermal maintaining a temperature of T_{wall}. The dimensions of cavities with various aspect ratios (AR, defined as the ratio of height to width of the cavity) simulated in the present study are given in Table 2. The list of various simulation conditions is given in Tables 3 and 4.

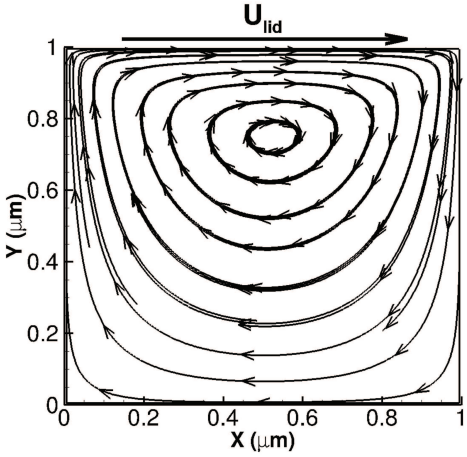

Figure 3: Cavity geometry.

Table 2: Dimensions in microns for wide and narrow cavities.

AR	**Height**	**Width**
1.0	1.0	1.0
0.4	1.0	2.5
2.5	2.5	1.0

Table 3: Simulation parameters for validation cases.

AR	Kn_{global}	$Mach_{lid}$	$T_{wall}\ (K)$
1.0	0.05	0.3	300
1.0	0.5	0.3	300
1.0	1.0	0.3	300
1.0	10.0	0.3	300

Table 4: Simulation parameters for studies on cavity flow physics.

AR	Kn_{global}	$Mach_{lid}$	$T_{wall}\ (K)$
0.4	0.005	0.3	273
0.4	0.05	0.3	273
0.4	1.0	0.3	273
0.4	10.0	0.3	273
0.4	0.005	3.0	273
0.4	0.05	3.0	273
0.4	1.0	3.0	273
0.4	10.0	3.0	273
2.5	0.005	0.3	273
2.5	0.05	0.3	273
2.5	1.0	0.3	273
2.5	10.0	0.3	273
2.5	0.005	3.0	273
2.5	0.05	3.0	273
2.5	1.0	3.0	273
2.5	10.0	3.0	273

DSMC Implementation

The grid spacing in any direction is one hundredth of a micron for DSMC simulations so that the cell size in never more than the freestream mean-free path (λ_∞).The time step for DSMC calculations is on the order of mean collision time of the freestream molecules, τ_∞ and intrinsic gas properties such as freestream number density (n_∞), λ_∞ and mean collision time (τ_∞) are calculated assuming a Variable Hard Sphere (VHS) binary collision

Table 5: Molecular properties for Argon gas.

Molecular mass, m	$66.3\times10^{-27}kg$
Reference diameter, d_{ref}	$4.17\times10^{-10}m$
Reference temperature, T_{ref}	$273K$
Viscosity index, ω_{VHS}	0.81
Diffusion index, α_{VHS}	1.0

model (Table 5, Eq. (3.2), Eq. (3.3))

$$\lambda_\infty = \frac{1}{\sqrt{2}\pi d_{ref}^2 n_\infty}, \tag{3.2}$$

$$\tau_\infty = \frac{1}{\pi d_{ref}^2 n_\infty \bar{c}_{r\infty}}, \tag{3.3}$$

where $\bar{c}_{r\infty}=\left(\frac{16kT_{ref}}{\pi m}\right)^{1/2}$ is the mean magnitude of the relative velocity of colliding molecules in freestream condition [9]. DSMC models the gas-boundary interaction using diffuse reflection model with complete thermal accommodation. The fraction determining number of real molecules represented by a simulated molecule is defined such that the average number of simulated molecules per cell is 25. Simulations in 2-D physical space must be performed carefully. Apart from grid sensitivity studies, it is equally important to confirm that one is not missing to capture any three dimensional flow features. Possibility of 3-D effects are high in our case since we deal with highly non-equilibrium flows with multiple vortex structures. However, in the following part, it is seen that our flow structures are free from any 3-D effects ensuring accurate results with corresponding 2-D simulations. in order to maintain a good acceptance rate of the collision partners being selected from a particular cell, and also to make a meaningful statistical averaging among the molecules in a cell. Collisions are calculated based on Variable Hard Sphere (VHS) binary collision model.

UGKS implementation

Based on grid sensitivity studies, the grid size for the UGKS computations was chosen to be 0.09 microns. The time-step is calculated from the CFL condition with a CFL number of 0.9. The Prandtl number is set to 2/3. A set of 28 weights based on Gauss-Hermite quadrature is used for numerical integration over the discrete velocity space in each direction [15]. The mean collision time (τ) for each cell is defined as the ratio its corresponding dynamic viscosity based on a VHS binary collision model (μ_{VHS}) to the macroscopic pressure (p)

$$\tau = \frac{\mu_{VHS}}{p}, \tag{3.4}$$

$$p = \frac{1}{3}\int \left((u-U)^2+\zeta^2\right) f d\Xi, \tag{3.5}$$

and μ_{VHS} is given by Sutherland's law

$$\mu_{VHS} = \mu_{ref}\left(\frac{T}{T_{ref}}\right)^{\omega_{VHS}}, \tag{3.6}$$

where μ_{ref} for VHS collision model is given by [9]

$$\mu_{ref} = \frac{5(\alpha_{VHS}+1)(\alpha_{VHS}+2)\sqrt{\pi}}{4\alpha_{VHS}(5-2\omega_{VHS})(7-2\omega_{VHS})} Kn_{global}. \tag{3.7}$$

The diffuse-wall boundary condition in UGKS is realised from the logic of impermeability condition. A particular computational cell attached to the left wall is considered for illustration purpose. The no-penetration condition then demands that

$$\sum_{k:\ u_k>0} u_k f^{(0)}_{w,k} + \sum_{k:\ u_k<0} u_k f^{in}_{w,k} = 0, \tag{3.8}$$

$f^{(0)}_{w,k}$ is the Maxwellian-type distribution function at the wall in the k^{th} velocity space

$$f^{(0)_{w,k}} = \rho_w \left(\frac{\lambda_w}{\pi}\right)^{\left(\frac{K+1}{2}\right)} e^{-\lambda_w\left((u_k-U_w)^2+\zeta^2\right)}, \tag{3.9}$$

where the subscript w denotes that the properties are at the wall. $f^{in}_{w,k}$ is the incoming distribution function from the right side of the wall-interface which is obtained based on a one-sided interpolation from the interior region. Density at the wall ρ_w is then computed from Eq. (3.8) to satisfy the impermeability condition. The corresponding Maxwellian distribution at the wall can then be calculated from Eq. (3.9). The distribution function at this boundary is then expressed as

$$f_{w,k} = \begin{cases} f^{(0)_{w,k}}, & \text{if } u_k \geq 0, \\ f^{in}_{w,k}, & \text{if } u_k < 0. \end{cases} \tag{3.10}$$

Finally, the fluxes $\boldsymbol{F_w}$ across the walls can be obtained from usual procedure

$$\boldsymbol{F_w} = \int_{t^n}^{t^{n+1}} \int \boldsymbol{\psi} f u d\Xi dt. \tag{3.11}$$

4 Results and discussion

The main objective of this study is to provide numerical verification of the UGKS-WENO implementation. Such verification can be most conveniently established in 2-D simulations.Due to relatively low computational burden, wide range of verifications can be performed with 2-D simulations. As a first step, we compare 2D simulations with 3-D

computations to establish that the former can capture important aspect of flow physics seen in the latter. Thus, we perform a comparison between 2-D and 3-D simulation results before proceeding to a more exhaustive verification/validation study with only 2-D simulations. Finally, we present on set of results for $100x100$ discrete velocity Newton-Cotes quadrature scheme.

4.1 Comparison between 2-D and 3-D simulations

A microcavity simulation of the case with lid velocity of $Mach = 0.3$ and $Kn = 10$ is performed in 3-D domain with periodic boundary conditions in the spanwise dimension (Z). The simulation is performed using OpenFOAM. The domain is divided into $100x100x100$ sampling cells. Fig. 4(a) shows the mean-velocity profiles along mid-horizontal and mid-vertical lines at different Z-planes. These profiles are also compared with corresponding 2-D DSMC and 2-D UGKS simulations in Fig. 4(a). Absence of any 3D effects is clearly seen since the mean-profiles are the same with each and every case. Figs. 4(b), 4(c) and

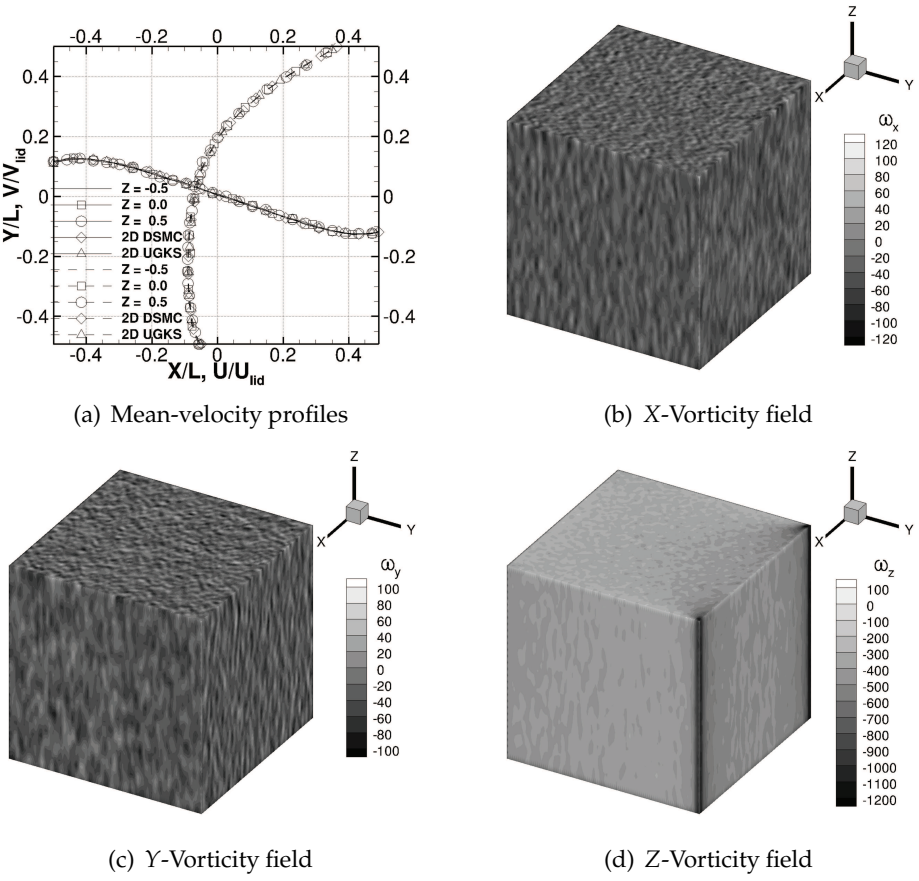

(a) Mean-velocity profiles

(b) X-Vorticity field

(c) Y-Vorticity field

(d) Z-Vorticity field

Figure 4: 3-D Effects.

4(d) show the x, y and z vorticity contours respectively. Note that the x and y vorticity fields are purely random and distributed symmetrically over the entire domain. Also, their average magnitude is very small compared to z-vorticity field. This clearly indicates that 2-D simulations can indeed capture aspects of 3-D flow physics. Through the remainder of this section, we will restrict ourselves to 2-D simulations for the verification and flow physics studies.

4.2 Verification results

Basic verifications of UGKS has been performed in [2]. It is shown that the scheme performs well in continuum and rarefied regimes. Here, we extend the validation to a larger range of Knudsen numbers. To enable this wider range, different WENO interpolation schemes are investigated.

The results from Van-Leer and WENO computations are compared against those from DSMC computations of (a) OpenFOAM (dsmcFOAM) and (b) the results of Mohammadzadeh et al. [16].

Figs. 5, 6, 7 and 8 show that the velocity and temperature profiles (along the mid-vertical line, mid-horizontal line and lid surface) generated by UGKS agrees well with those of corresponding DSMC simulations. Slight deviations in temperature profiles of DSMC from that of UGKS at low global Knudsen numbers (Figs. 7 and 8) can be attributed to the inadequacies (of cell-size, time-step and the number of particles per cell) of DSMC at near continuum regime. Such slight deviations (owing to the large cell size) have also been reported in DSMC simulations were carried out in continuum regime to obtain flow fields in an expanding jet [17]. The main advantage of UGKS over DSMC at low Knudsen numbers is also evident from the computational time required for the simulations. For low global Kn numbers, DSMC simulations with openFOAM were at least ten times computationally more expensive than a corresponding UGKS based simulation.

As can be seen from Figs. 5, 6 and 7, UGKS with Van-Leer scheme shows undesirable oscillations, that become prominent at high Knudsen numbers. These spurious oscillations are eliminated when higher order WENO reconstruction scheme is employed. Moreover, at higher Knudsen numbers, UGKS with Van-Leer scheme has a much slower rate of convergence compared to WENO-S or WENO-C schemes. A better illustration of the smoothing effect of WENO schemes can be seen by comparing Fig. 9 and Fig. 10, which show the temperature contours overlaid with the heat-flux lines (coloured with heat-flux magnitude). Detailed discussion on the origination and possible means of removal of these non-physical oscillations are included in Section **??**. The inference is that UGKS with a WENO-based reconstruction scheme is necessary at high Knudsen number regimes. WENO-S and WENO-C produce nearly identical profiles for velocity and temperature. Also, it is noted that these two schemes give similar steady-state values for all macroscopic properties throughout the domain. The main distinction between the two WENO methods is in the rate of convergence. WENO-C leads to a more rapid conver-

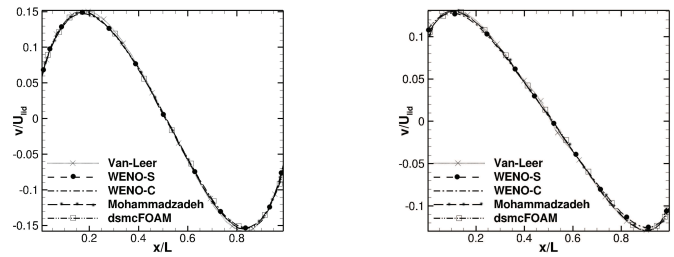

(a) $Kn=0.05$ (b) $Kn=0.5$

(c) $Kn=1.0$ (d) $Kn=10.0$

Figure 5: V-velocity profile al4ong mid-horizontal line.

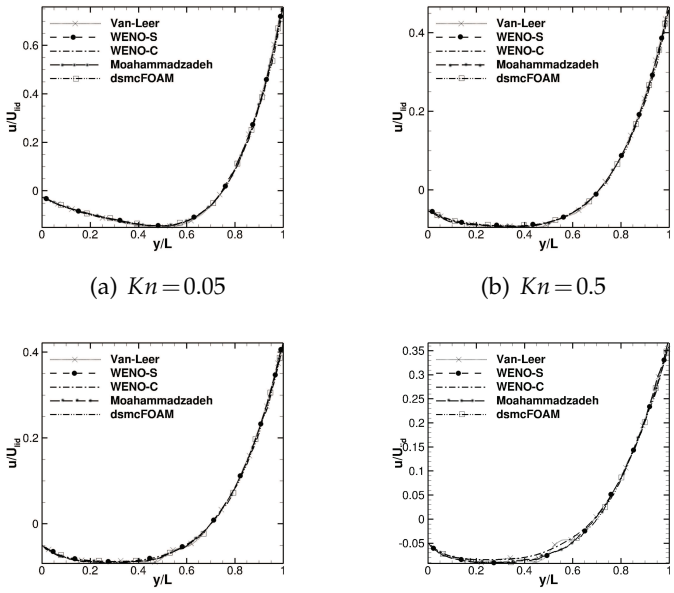

(a) $Kn=0.05$ (b) $Kn=0.5$

(c) $Kn=1.0$ (d) $Kn=10.0$

Figure 6: U-velocity profile along mid-vertical line.

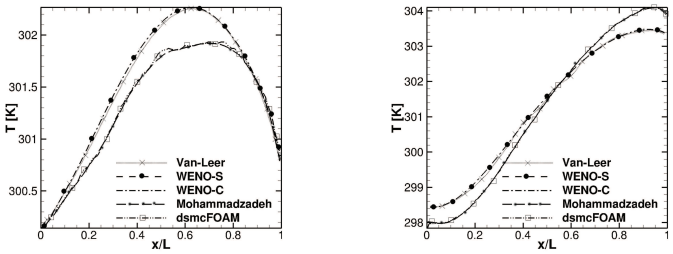

(a) $Kn=0.05$ (b) $Kn=0.5$

(c) $Kn=1.0$ (d) $Kn=10.0$

Figure 7: Temperature profile along mid-horizontal line.

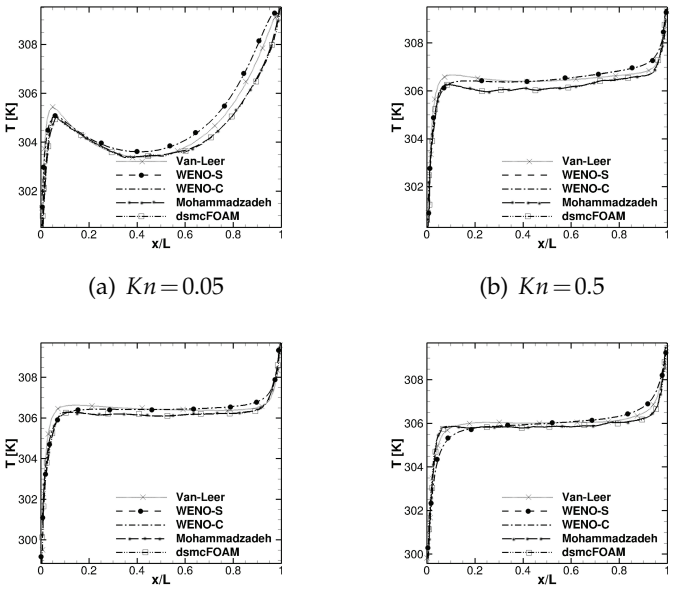

(a) $Kn=0.05$ (b) $Kn=0.5$

(c) $Kn=1.0$ (d) $Kn=10.0$

Figure 8: Temperature profile along the lid.

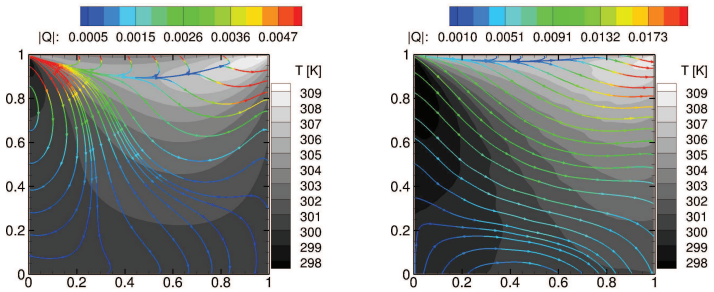

(a) $Kn=0.05$

(b) $Kn=0.5$

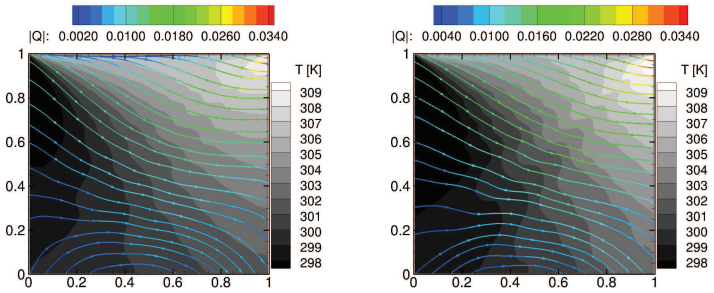

(c) $Kn=1.0$

(d) $Kn=10.0$

Figure 9: Temperature contours overlaid with heat-flux lines (Van-Leer).

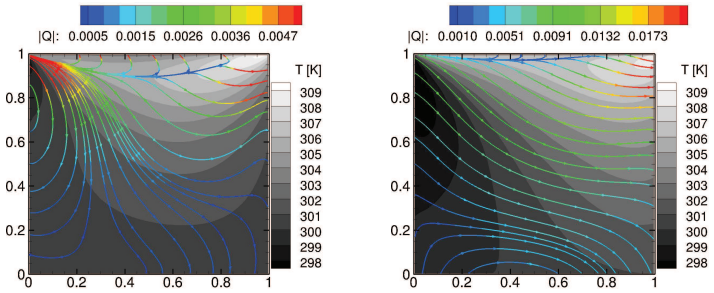

(a) $Kn=0.05$

(b) $Kn=0.5$

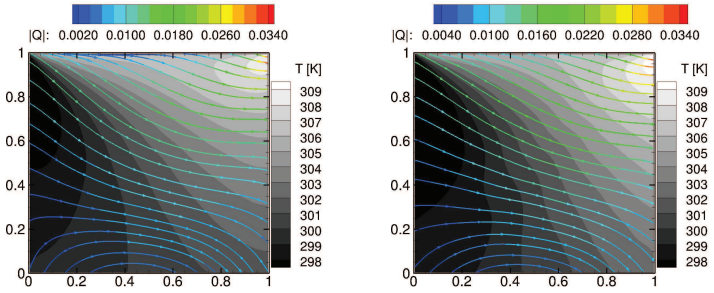

(c) $Kn=1.0$

(d) $Kn=10.0$

Figure 10: Temperature contours overlaid with heat-flux lines (WENO-S).

gence. However, WENO-C is computationally expensive since it uses an extra stencil to interpolate the flux data to the cell interface. Throughout the reminder of this article, we present results from WENO-S which was found to be adequate for current simulations.

4.3 Micro-cavity flow physics

Micro-cavities of practical interest come in many shapes and sizes. The nature of flow inside these cavities depend critically on the shape. To understand the influence of shape, we simplify the cavity geometry to rectangles of different aspect ratios shown in Table 2. Flows within these cavities are simulated at different Mach and Knudsen numbers, and the results are examined.

Figs. 11, 12, 13 and 14 show the streamlines coloured with the normalized velocity magnitude for wide and deep cavities at different Knudsen and Mach numbers. The background contour illustrates the varying strength of z-vorticity normalized by U_{lid}/L.

Note that the contour levels for z-vorticity are set in logarithmic scale indicating a large range of z-vorticity strength (of about 10 orders of magnitude) within the cavity. Comparison between these sets of figures reveal important Mach and Knudsen number effects.

It can be clearly seen that a wide cavity, on an average, has a higher stream-wise velocity as well as z-vortex strength when compared to a similar case (of same Knudsen and Mach numbers) with a deep cavity. However, this behaviour is expected since the rate at which momentum gets transferred from the moving lid to molecules within the cavity is high for wide cavities owing to its large lid stroke for given area. Thus, the lid transfers more momentum to the cavity fluid. The flow in wide cavities approach steady state more readily and exhibit a stable configuration involving a single large primary vortex. This was not the case with deep cavities where in most of the simulations triggered the formation of a second vortex.

At a constant lid velocity, the number of active vortices decrease with an increase of global Knudsen number. The mechanism that creates additional vortices for flows near continuum regimes is clearly demonstrated in Figs. 12(b) and 14(b). It is seen that for $AR=0.4$ (Fig. 12(b)), secondary eddies have been created at the two bottom corners under the main vortex. As the aspect ratio is increased to 2.5, these secondary eddies grow and merge into a second vortex under the main one.

When the Knudsen number is maintained constant, the number of vortices increase with an increase in the lid velocity. This is more prominent with flows in near-continuum regime and with a high cavity aspect ratio. An interesting observation is that of the large difference in vortex strengths between the vortices which appeared in a particular flow. It is noted that the multi-vortex configuration is stable when secondary or higher level vortices progressively showed a large relative difference in their vortex strengths. However, at high lid velocities, higher order vortices with vortex strengths comparable to the primary vortex start appearing with an increase in the degree rarefaction (Fig. 14). This phenomena triggers numerical instability (see Section **??**) with non-physical oscillations

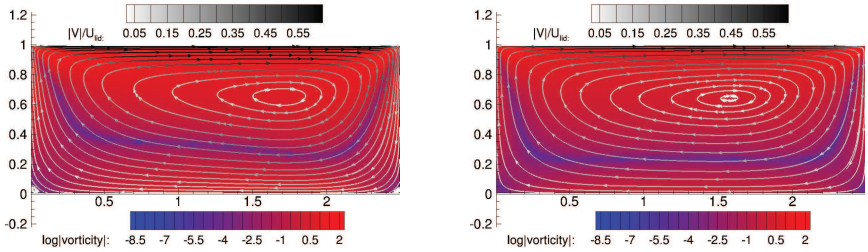

(a) $Kn=0.005$ (b) $Kn=0.05$

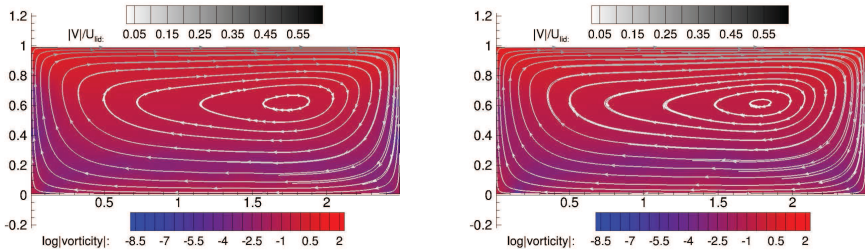

(c) $Kn=1$ (d) $Kn=10$

Figure 11: Vortex structures for $AR=0.4$, $Mach_{lid}=0.3$.

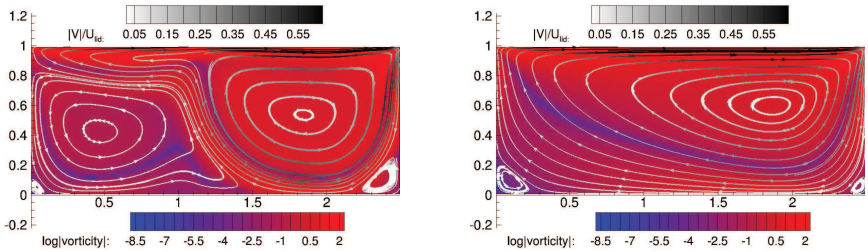

(a) $Kn=0.005$ (b) $Kn=0.05$

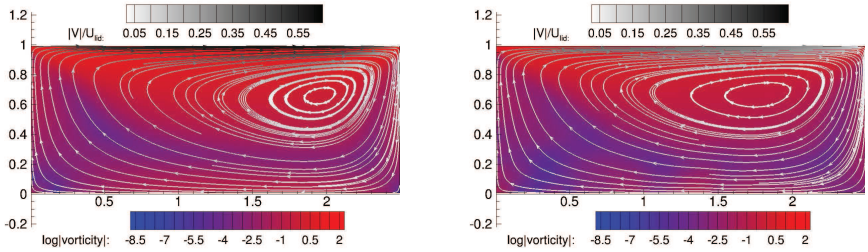

(c) $Kn=1$ (d) $Kn=10$

Figure 12: Vortex structures for $AR=0.4$, $Mach_{lid}=3.0$.

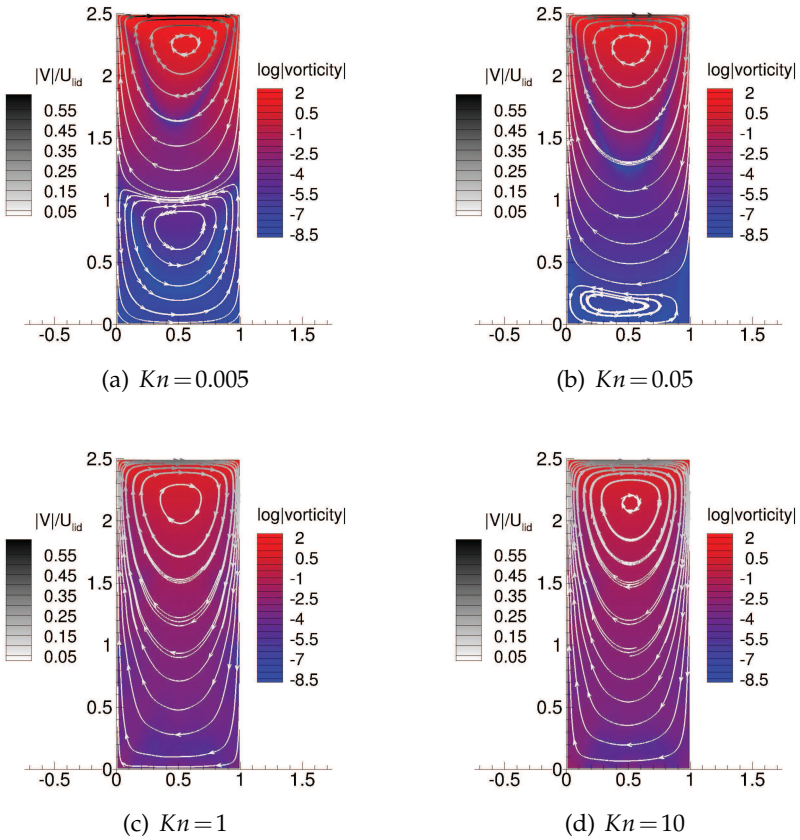

(a) $Kn=0.005$ (b) $Kn=0.05$

(c) $Kn=1$ (d) $Kn=10$

Figure 13: Vortex structures for $AR=2.5$, $Mach_{lid}=0.3$.

in the flow affecting the rate of convergence. For example, a snapshot of the highly non-equilibrium case can be seen in Fig. 14(d). However, when the aspect ratio is reduced for the same case (Fig. 12(d)), the geometry combined with the high degree of rarefaction disallows the formation of any secondary eddies henceforth causing the flow to be steady and stable with a single vortex configuration.

Another important factor to be noted from Fig. 10 is that the temperature peaks on the upper right corner of the cavity, which increases with an increase in the degree of rarefaction. This phenomena can be attributed to the relatively lesser number of inter-molecular collisions (which allows for an exchange in energy transfer to neighbouring molecules) than the number of molecular-surface interactions that occur in a rarefied cavity flow. Further, the direction of heat flux disobeys Fourier's law particularly with an increase in the degree or rarefaction. Wang et al. [18] has derived an empirical model for non-Fourier heat transfer by examining DSMC data of rarefied hypersonic flows. However, a universal model is yet to be formulated. A detailed study with an extended set of simulations is currently under progress.

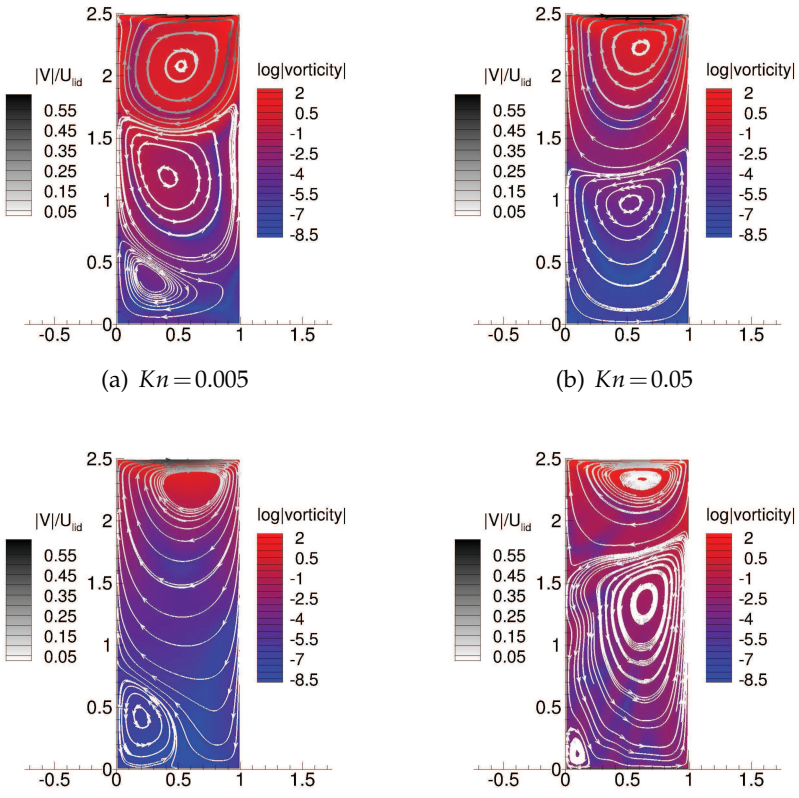

(a) $Kn=0.005$ (b) $Kn=0.05$

(c) $Kn=1$ (d) $Kn=10$

Figure 14: Vortex structures for $AR=2.5$, $Mach_{lid}=3.0$.

4.4 Simulations with Newton-Cotes quadrature

Due to the discretization in the velocity space, UGKS suffers from boundary induced discontinuities at high Knudsen numbers. A typical feature of the cavity flow is that the distribution function can become highly irregular from discontinuities induced around its corners. Significant oscillations are induced by the top two corners of the cavity due to the strong discontinuities in the velocity between stationary and moving walls. The discontinuities from the boundaries propagate inside the computational domain and produce non-physical oscillatory behaviour in the macroscopic quantities. The issue is popularly known as 'ray effects' in the transport theory community and appears in neutron transport and radiative transfer [19]. Methodologies have been proposed and successfully implemented to eliminate this problem for low-speed rarefied flows [20, 21]. The 'ray effects', in general, can be partially eliminated by increasing the number of discrete velocities. With such an approach, the amplitude of these oscillations decreases but their frequency increases. Further, the Gauss-Hermite type distribution points are

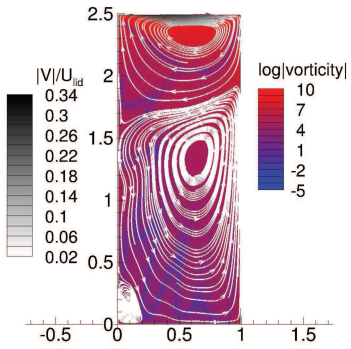

(a) Van-Leer with 100×100 velocity points

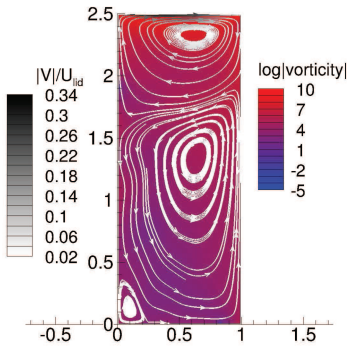

(b) WENO-S with 100×100 velocity points

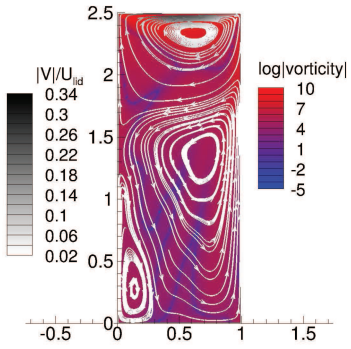

(c) Van-Leer with 100×100 velocity points

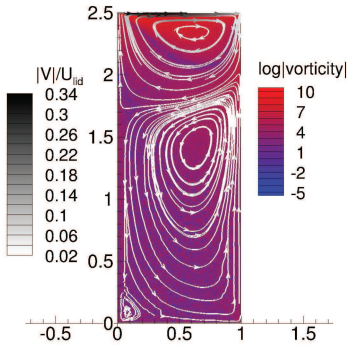

(d) DSMC

Figure 15: Vortex structures for $AR=2.5$, $Mach_{lid}=3.0$, $Kn=10$.

widely spaced in the velocity space. The weights of extreme velocities can be rather small, minimizing their contribution in the process of numerical integration. So, the use of Newton-Cotes quadrature is more promising in rarefied supersonic flows which are in high non-equilibrium state [22].

In this final study, simulations are performed with an increased number of discrete velocity points. Simulations are performed with a 100×100 Newton-Cotes quadrature for the highly non-equilibrium case of deep cavity with a lid velocity of *Mach* 3 and *Kn* 10. UGKS simulations with both Van-Leer and WENO-S interpolations are performed and are compared with a corresponding DSMC simulation. Fig. 15 shows the vortex structures generated by these computations. Simulation with WENO-S converge much faster than a corresponding Van-Leer case. Figs. 15(a), (b) and (d) shows the converged steady solutions. Figs. 15(b) and 15(b) are converged solutions to the same convergence criteria, but the latter took almost double the number of iterations more to reach a steady-state solution (Fig. 15(a)). The DSMC solution (Fig. 15(d)) is oscillation-free and is believed to be the most accurate in this rarefied supersonic regime. It can be seen that both Figs. 15(a)

and 15(b) yield similar vortex structures to those by DSMC. However, the non-physical oscillations in streamlines as well as the vorticity contours (Figs. 14(d) and 15(a)) are smoothed out by the WENO-S based UGKS simulation (Fig. 15(b)).

5 Concluding remarks

The results from UGKS codes are validated against corresponding DSMC solutions for a wide range of Knudsen numbers spanning from near-continuum/slip regime to rarefied regime. Use of WENO schemes for initial reconstruction of the distribution fluxes gave oscillation free solutions with higher spacial accuracy as well as faster convergence compared to Van-Leer limiting scheme at high Knudsen numbers.

Further simulations with varying aspect-ratio reveals that the formation of secondary vortices depend on the degree of rarefaction as well as the lid velocity. It is observed that multi-vortex configurations are favourable in high aspect ratio cavities. As the degree of rarefaction is increased, secondary vortices tend to disappear. At the same time, the number of active vortices increase with an increase in the lid velocity. However, with higher lid velocities at highly rarefied regimes, non-physical oscillations appear in the flow domain. Newton-Cotes quadrature with 100 velocity points in each direction along with a 5^{th} WENO scheme for flux interpolation is then necessary to obtain a physically meaningful steady-state with UGKS. Full 3-D simulations are needed to further confirm the physical features presented here.

References

[1] J. J. Bertin and R. M. Cummings, Critical Hypersonic Aerothermodynamic Phenomena, Annual Review of Fluid Mechanics 38: 129-157, Jan 2006.
[2] K. Xu and J. C. Huang, A unified gas-kinetic scheme for rarefied and continuum flows, J. Comp. Phy. 229, 7747-7764, 2010.
[3] E.M. Shakhov, Generalization of the Krook kinetic equation, Fluid Dyn. 3: 95, 1968.
[4] P.L. Bhatnagar, E.P. Gross, M. Krook, A model for collision processes in gases I: small amplitude processes in charged and neutral one-component systems, Phys. Rev. 94: 511525, 1954.
[5] J.Y. Yang, J.C. Huang, Rarefied flow computations using non-linear model Boltzmann equations, J. Comput. Phys. 120: 323339, 1995.
[6] Chi-Wang Shu, Essentially Non-Oscillatory and Weighted Essentially Non-Oscillatory schemes for hyperbolic conservation laws, NASA/CR-97-206253, ICASE Report No. 97-65, 1997
[7] N. K. Yamaleev, M. H. Carpenter, Higher order energy stable WENO schemes, 47th AIAA Aerospace Sciences Meeting, Orlando, FL, USA, 2009.
[8] B. Van Leer, Towards the ultimate conservative difference scheme V. A second order sequel to Godunov's method, J. Comp. Phys. 32: 101136, 1979.
[9] G. A. Bird, Molecular Gas Dynamics and the Direct Simulation of Gas Flows, Oxford Science Publications, 1994.

[10] K. Xu, Gas-Kinetic Schemes for Unsteady Compressible Flow Simulations, von Karman Institute for Fluid Dynamics, Lecture Series 1998-03, 29th Computational Fluid Dynamics, (Feb. 23-27, 1998).
[11] Z. Guo, K. Xu, Ruijie Wang, Discrete unified gas kinetic scheme for fluid dynamics: I. Isothermal smooth flows, May 2013.
[12] J. Kerimo and S. S. Girimaji, DNS of decaying isotropic turbulence with Boltzmann BGK approach, J. Turb. 46 (8): 1-16, 2007.
[13] G. Kumar and S. S. Girimaji, WENO-enhanced Gas Kinetic Method for highly compressible transition and turbulence simulations, J. Comp. Phys. 234 (1): 499-523, 2013.
[14] K. H. Prendergast, K. Xu, Numerical hydrodynamics from gas kinetic theory, J. Comp. Phys. 109(1): 5366, 1993.
[15] B. Shizgal, A Gaussian quadrature procedure for use in the solution of the Boltzmann equation and related problems, J. Comp. Phys. 41: 309328, 1981. doi:10.1016/0021-9991(81)90099-1
[16] A. Mohammadzadeh, E. Roohi, H. Niazmand, A Parallel DSMC Investigation of Monatomic/Diatomic Gas Flows in a Micro/Nano Cavity,Numerical Heat Transfer, Part A 63:4, 305-325, 2013.
[17] T. J. Bartel, T. M. Sterk, J. L. Payne, B. Preppernau, DSMC Simulation of Nozzle Expansion Flow Fields, 6^{th} AIAA/ASME Joint Thermophysics and Heat Transfer Conference June 20-23, 1994.
[18] Z. Wang, L. Bao, B. Tong, Rarefaction criterion and non-Fourier heat transfer in hypersonic rarefied flows, Physics of Fluids 22, 126103, 2010.
[19] E.E. Lewis, W.F. Miller Jr., Computational Methods in Neutron Transport Theory, Wiley, 1984.
[20] S. Naris and D. Valougeorgis, The driven cavity flow over the whole range of the Knudsen number, Physics of Fluids 17, 097106, 2005
[21] S. Varoutis, D. Valougeorgis, F. Sharipov, Application of the integro-moment method to steady-state two-dimensional rarefied gas flows subject to boundary induced discontinuities, J. Comp. Phys. 227: 6272-6287, 2008.
[22] Z. Guo, K. Xu, R. Wang, Discrete unified gas kinetic scheme for all Knudsen number flows: Low-speed isothermal case, Physical Review E 88, 033305, 2013.